Growth of Single- and Bilayer ZnO on Au(111) and Interaction with Copper

Xingyi Deng,*[†,§,∥] Kun Yao,[‡,∥] Keju Sun,[‡] Wei-Xue Li,*[‡] Junseok Lee,[†,§] and Christopher Matranga[†]

[†]National Energy Technology Laboratory (NETL), United States Department of Energy, P.O. Box 10940, Pittsburgh, Pennsylvania 15236, United States

[‡]State Key Laboratory of Catalysis, Dalian Institute of Chemical Physics, Chinese Academy of Sciences, Dalian 116023, China

[§]URS, P.O. Box 618, South Park, Pennsylvania 15129, United States

Ⓢ *Supporting Information*

ABSTRACT: The stoichiometric single- and bilayer ZnO(0001) have been prepared by reactive deposition of Zn on Au(111) and studied in detail with X-ray photoelectron spectroscopy, scanning tunneling microscopy, and density functional theory calculations. Both single- and bilayer ZnO(0001) adopt a planar, graphite-like structure similar to freestanding ZnO(0001) due to the weak van der Waals interactions dominating their adhesion with the Au(111) substrate. At higher temperature, the single-layer ZnO(0001) converts gradually to bilayer ZnO(0001) due to the twice stronger interaction between two ZnO layers than the interfacial adhesion of ZnO with Au substrate. It is found that Cu atoms on the surface of bilayer ZnO(0001) are mobile with a diffusion barrier of 0.31 eV and likely to agglomerate and form nanosized particles at low coverages; while Cu atoms tend to penetrate a single layer of ZnO(0001) with a barrier of 0.10 eV, resulting in a Cu free surface.
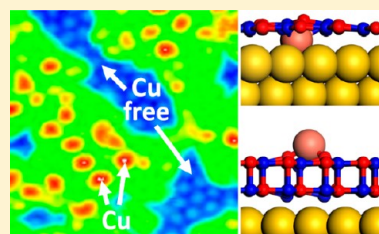
INTRODUCTION

Oxides exist abundantly in nature, and the controlled surface growth of oxide materials is of broad interest across many fields such as spintronics,[1] display applications,[2] and catalysis.[3] In comparison with corresponding bulk or thick film materials, oxide films and nanostructures containing only a few atomic layers, namely, ultrathin oxide materials, have novel characteristics originating from interfacial and finite size effects.[4] An example of this effect is MoO_3, which crystallizes in a bilayer bulk structure, whereas its nanostructures on Au(111) possess a unique single-layer architecture with Au playing the stabilizing role of the missing half of the bilayer.[5] Additionally, it has been shown that Au grows two-dimensionally on ultrathin MgO films and wets the surface, whereas it grows in a three-dimensional fashion on thicker films.[6] Exploring and understanding the characteristics of these surface grown ultrathin oxide materials are needed to further advance their applications in microelectronics and heterogeneous catalysis.[4a]

Recently, zinc oxide (ZnO) has attracted interest due to its use in photovoltaics, light emitting devices, gas sensors, and catalysis.[7] Developing a fundamental understanding of ZnO surface structures and their properties has become an active subject for investigation. Bulk ZnO crystallizes in the wurtzite structure with its two notable polar surfaces, i.e., ZnO(0001)-Zn and ZnO(000$\bar{1}$)-O, undergoing modification or reconstruction to compensate for the energy cost arising from the nonvanishing dipole moment.[8] Distinct from the bulk phase, ultrathin ZnO(0001) emerges with a film-specific structure with a novel depolarization mechanism. Theoretically, it has been suggested that a freestanding ultrathin ZnO(0001) layer would transform to a planar, graphite-like structure.[9] Ultrathin

ZnO(0001) (up to two atomic layers) grown on Ag(111) indeed adopts this unique nonpolar structure.[10] More recently, ultrathin ZnO on Pd(111) has been shown to be either H-terminated Zn_6O_5 or graphite-like Zn_6O_6 depending on the oxygen pressures used to prepare the oxide.[11] It is unclear yet what is the role of the substrate for the structure of the grown ultrathin ZnO, in particular how important the interaction between the substrate and grown ultrathin ZnO as well as its interplay with the interaction between ZnO layers dictates the structures and wetting behavior of the surface grown ultrathin ZnO. The fundamental understanding gained would provide valuable insight on the surface growth of oxide materials at reduced dimensionality. Since the grown ultrathin oxides with different thickness might have distinct electronic and structural properties to influence their surface chemistry toward many adsorbates,[12] it is also interesting to know how the ultrathin ZnO as a support interacts with metals such as copper as well as its dependence on film thickness. This would provide an ideal model system to mimic the composition of the popular Cu/ZnO catalysts for the water gas shift (WGS) and methanol synthesis.[13]

To address these questions, we employ in this work a combination of experimental and theoretical approaches to investigate the growth of the ultrathin ZnO on Au(111) and its interaction with Cu. The Au(111) surface is selected as a substrate to exploit its inertness toward many oxidants such as O_2 and NO_2. We find that single- or bilayer ZnO(0001) can be
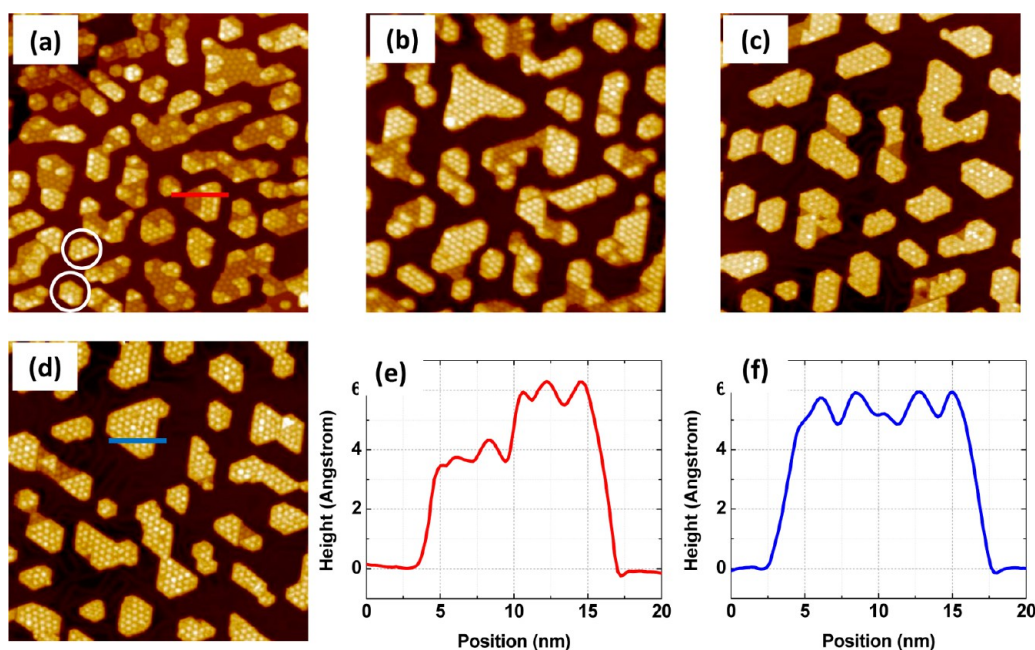
Figure 1. Room temperature STM images (I = 5 pA, V = 1.5 V, 100×100 nm^2) of 0.9 MLE ZnO grown on Au(111) using the reactive deposition method described in the text followed by annealing at 550 K for (a) 5; (b) 30; (c) 60; and (d) 120 min. (e,f) Linescans specified in panels a and d, respectively.

prepared on Au(111) with the interfacial adhesion energy dominated by weak van der Waals interactions. As such, both adopt a planar, graphite-like structure similar to that of freestanding ZnO(0001) to minimize the surface polarity originating from stacking the opposite charged atomic layers.[9b] The interaction between two ZnO(0001) layers is found to be almost twice of that between a ZnO(0001) layer and the Au(111) substrate, driving the conversion of the single-layer ZnO(0001) to bilayer ZnO(0001) at high temperature. In addition, we find completely different energetics and properties associated with the adsorption of Cu on the single- and bilayer ZnO(0001), demonstrating that the thickness as a controllable dimension could dictate characteristics of an ultrathin oxide material.

EXPERIMENTAL AND THEORETICAL METHODS

All experiments were carried out in a commercial ultrahigh vacuum (UHV) chamber from Omicron Nanotechnology GmbH. This chamber is equipped with scanning tunneling microscopy (STM), X-ray photoelectron spectroscopy (XPS), low-energy electron diffraction (LEED), and low-energy ion scattering (LEIS). The base pressure was maintained at ~1 × 10^{-10} mbar. The growth of ZnO on Au(111) was achieved by the reactive deposition, referring to the evaporation of Zn onto Au(111) in the presence of NO$_2$ ($P = 3 \times 10^{-8}$ mbar) at room temperature followed by annealing at 550 K in UHV. Zn was evaporated using an electron-beam assisted evaporator (Omicron EFM3T) from a rod material (Goodfellow, 2.0 mm diameter, 99.99%) at 450 V with emission current ~1.5− 1.6 mA. NO$_2$ (Research grade) was used as received and without further purification. Note that the reactive deposition with O$_2$ at pressure up to 2×10^{-6} mbar was unable to fully oxidize Zn (data not shown). Prior to the growth of ZnO, the Au(111) single crystal (10×10 mm^2, Princeton Scientific Corp.) was cleaned by cycles of Ar$^+$ sputtering ($P = 2 \times 10^{-6}$ mbar, 1.5 keV) at 300 K, followed by annealing at 700 K for 10

min. The coverage of ZnO on Au(111) is noted as a monolayer equivalent (MLE), referring to the atomic ratio of Zn (or O) in the oxide to the surface Au.[14] The MLE coverage was determined from the XPS data using the Zn 3s (or O 1s) and Au 4f peaks, with corrections made for the atomic sensitivity factors (ASF) and the inelastic mean free path (IMFP), as described in our previous study.[15] It gives relative coverage values of ZnO on Au(111) in this work rather than providing absolute values. The reference ZnO single crystals, i.e., ZnO(0001)-Zn and ZnO(000$\bar{1}$)-O (MTI Corporation), were cleaned by cycles of Ar$^+$ sputtering ($P = 2 \times 10^{-6}$ mbar, 1.0 keV) at 300 K, followed by annealing at 750 K for 5 min until no contaminants, such as C, were detected using XPS. XPS measurements were performed using a MgKα X-ray source (1253.6 eV, 300 W) and a hemispherical analyzer with pass energy of 20 eV at room temperature. The binding energy was calibrated with the Au 4f$_{7/2}$ peak at 83.8 eV for each spectrum. All STM measurements were performed at room temperature in constant current mode using etched W tips purchased from Omicron. All STM images were plane-corrected using scanning probe imaging processor (SPIP, Imagemet) software.

Density functional theory (DFT) calculations were performed using Vienna Ab-initio Simulation Package (VASP),[16] employing the all-electron projected augmented wave (PAW) potentials.[17] The exchange-correlation functional was described by optB88-vdW functional,[18] which is important in the accurate description of the van der Waals interaction between ZnO and Au(111). The correction of the on-site Coulomb repulsion for Zn was considered, and a value of $U - J = 8.5$ eV[19] was used in present work. We also tested the value of $U - J = 4.7$ eV[20] and found that both values gave rather similar structures and energetics as seen in Tables S4 and S5, Supporting Information. The wave functions were expanded by plane-wave basis with cutoff energy of 400 eV. The optimized Au lattice constant was 4.14 Å, agreeing well with the experimental value of 4.07 Å and
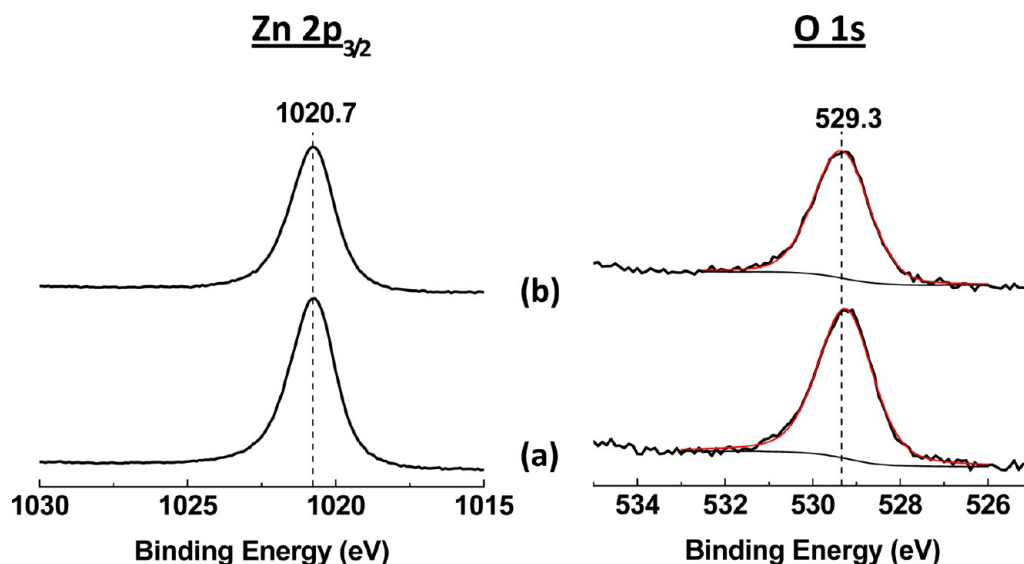
Figure 2. Zn 2p$_{3/2}$ and O 1s XP spectra of 0.9 MLE ZnO grown on Au(111) using the reactive deposition followed by annealing at 550 K for (a) 5 and (b) 120 min. Measurement T = 300 K. While both the Zn 2p$_{3/2}$ and O 1s XP peak intensities decrease slightly (<10%) with annealing time from 5 to 120 min, their ratios remain unchanged, suggesting that annealing at 550 K does not alter the stoichiometry of ZnO. The symmetric nature of the O 1s peaks also rules out the presence of a substantial amount of surface hydroxyl groups.

also the previous calculation value of 4.12 Å.[21] The ZnO/Au(111) Moiré pattern observed was simulated by a periodic slab of ZnO(0001)-(7 × 7)/Au(111)-(8 × 8) separated by a vacuum at least 10 Å at normal direction throughout the present work. The large supercell allowed using gamma point only to sample the surface Brillouin zone. Three-layer thick Au(111) slab was used since further increase of the slab thickness to four- and five-layer has negligible influence on the structure and energetics as seen in Tables S6 and S7, Supporting Information. The ZnO layer(s) and topmost Au layer were relaxed until the residual force less than 0.03 eV/Å. The transition states were calculated using climbing-image nudged elastic band (CI-NEB) method.[22] More than eight images including the initial state and final state were constructed and optimized until the force between each individual image less than 0.05 eV/Å. To compare with experimental observations, STM images of the optimized superstructure were simulated using the Tersoff–Hamann theory.[23]

■ RESULTS AND DISCUSSION

Ultrathin ZnO nanostructures were grown on Au(111) using reactive deposition at room temperature followed by annealing as described in the Experimental section. While determining the stoichiometry of a surface grown oxide is not a trivial task, a comprehensive analysis based on the X-ray photoelectron spectroscopy (XPS) quantification and comparison with the data from the ZnO single crystals unequivocally suggests that the reactive deposition produces stoichiometric ZnO on Au(111) (see Supporting Information for details). Briefly, the atomic ratio of Zn to O in the oxide grown on Au(111) is calibrated to be 1:1 using the integrated intensities of the Zn 3s and O 1s XP peaks with corrections for their respective cross-section values.[24] In addition, the XP peak ratio of the Zn 3s to O 1s in the ZnO on Au(111) agrees well with that in the ZnO single crystals (including both ZnO(0001)-Zn and ZnO(000$\bar{1}$)-O) after taking the escape depths of photoelectrons into account for the bulk materials.

Two types of ZnO nanostructures on the Au(111) surface with distinctive heights are revealed with scanning tunneling microscopy (STM). Figure 1a shows a typical STM image of 0.9 MLE ZnO on Au(111) prepared from the reactive deposition followed by annealing at 550 K for 5 min. The height of the lower ZnO structure (noted as the low-ZnO) in STM is measured to be ~3.5 Å, whereas the height of the high-ZnO is measured to be ~5.5 Å, based on the linescan shown in Figure 1e. The density of the low-ZnO is higher on the Au(111) surface at this preparation condition. On the basis of the STM images, we estimate this surface is composed of roughly 60% low-ZnO and 40% high-ZnO. The low-ZnO is always embedded in or bundled with the high-ZnO. However, pure high-ZnO structures were observed as highlighted in the circles in Figure 1a. Both ZnO structures show a hexagonal Moiré pattern on their surfaces with a periodicity of ~23 Å.

The low-ZnO on Au(111) is gradually converted to the high-ZnO upon annealing at 550 K for an extended period. Specifically, there appears more high-ZnO on Au(111) at the expense of the low-ZnO after annealing at 550 K for 30 min (Figure 1b). Estimates based on STM images indicate that this surface is composed of ~20% low-ZnO and ~80% high-ZnO. At the same time, the average size of the high-ZnO increases noticeably. After annealing at 550 K for 60 min, the high-ZnO becomes the more dominant species on Au(111) with fewer low-ZnO (<10%) structures embedded within the high-ZnO structure (Figure 1c). Further annealing at 550 K (i.e., for 120 min) does not induce significant change of the ZnO morphology (Figure 1d). The linescan shows that the height of the high-ZnO phase remains at ~5.5 Å (Figure 1f). In all cases, the Moiré patterns are always shown on the surfaces of the ZnO structures with the same periodicity. It should be noted that annealing at temperatures higher than 550 K, for instance 575 K, results in a quick loss of ZnO on Au(111) possibly due to the decomposition of ZnO or diffusion of ZnO into the bulk.

Regardless of the morphology change associated with the annealing, the ZnO nanostructures on Au(111) remain
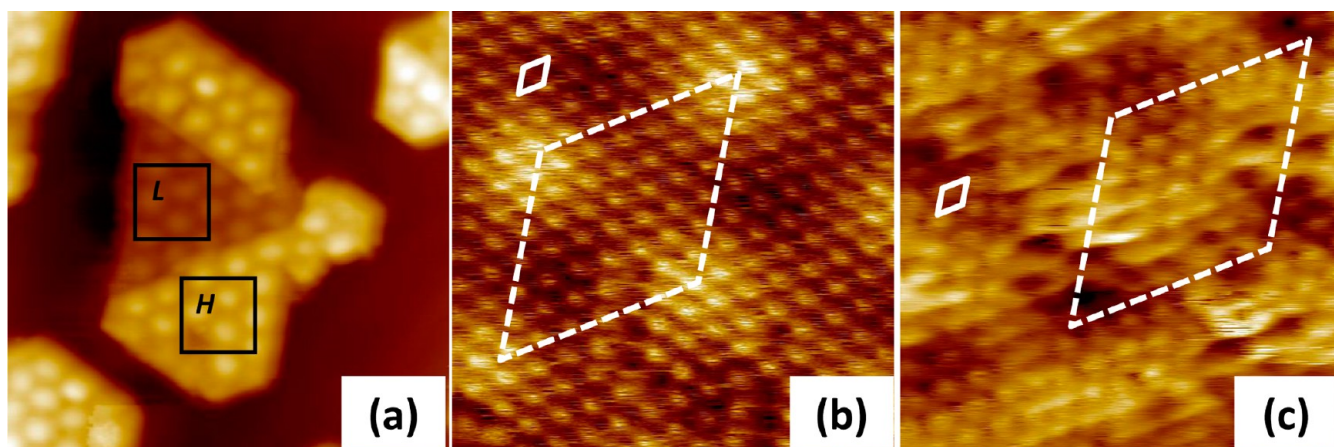
Figure 3. Room temperature STM images showing (a) details of both low- and high-ZnO structures grown on Au(111) (30×30 nm^2; $I = 5$ pA, $V =$ 1.5 V); (b) atomic structure of low-ZnO (5×5 nm^2; $I = 500$ pA, $V = 0.2$ V); (c) atomic structure of high-ZnO (5×5 nm^2; $I = 300$ pA, $V = 0.1$ V). The solid and the dashed cells in panels b and c indicate the repeating unit of ZnO ($\sim$3.3 Å) and the Moiré structure ($\sim$23 Å), which are in the same registry.

stoichiometric. The presence of ZnO on Au(111) is signified by a Zn $2p_{3/2}$ XP peak located at 1020.7 eV and also an O 1s peak at 529.3 eV (Figure 2). While both the Zn $2p_{3/2}$ and O 1s XP peak intensities decrease slightly (<10%) with annealing time from 5 to 120 min, their ratios are essentially unchanged. In addition, there is no measurable binding energy (BE) shift associated with this extended annealing time at 550 K, i.e., the BEs of the Zn $2p_{3/2}$ and O 1s peaks stay at 1020.7 and 529.3 eV, respectively. Importantly, the O 1s XP peaks are symmetric, which can be fitted with single component centered at 529.3 eV (red line), and there is no apparent component at BE = 530−531 eV, indicating that no substantial amount of hydroxyl groups (adsorbed OH) are present on the ZnO surfaces.

Atomically resolved STM images suggest that both the low-ZnO and the high-ZnO surfaces are similar in a hexagonal symmetry. Figure 3a shows a detailed image of ZnO on Au(111) with the hexagonal Moiré patterns seen on both low-ZnO and high-ZnO structures. STM also resolves a similar atomic structure on both ZnO structures consisting of a hexagonal unit cell with a lattice parameter of ~3.3 Å (Figure 3b,c). It can also be seen in these STM images the atomic unit cell and the Moiré repeating unit are in the same registry (highlighted by solid and dashed cells), indicating that the ZnO lattice is in alignment with the Au(111) lattice.

The structure and evolution of the grown ZnO nanostructures observed was studied by density functional theory (DFT) calculations. In the bulk wurtzite ZnO crystal, the O^{2-} anions form a hexagonal close-packed (HCP) sublattice with the Zn^{2+} anions occupying the interstitial tetrahedral positions. The (0001) facet in the wurtzite ZnO crystal is repeated by a hexagonal unit cell with a lattice constant of 3.25 Å, and the step height of two layers of ZnO(0001) is 5.2 Å. On the basis of our STM results, we have thus considered a single- and a bilayer ZnO(0001) from the bulk wurtzite structure as a starting point for structure optimization of the low-ZnO and high-ZnO in DFT, respectively. The observed Moiré patterns in STM were simulated by a ZnO(0001)-(7×7)/Au(111)-(8×8) supercell (Figure 4a) based on the calculated Au lattice constant using DFT. Corresponding lateral dimension of the superstructure (23.4 Å) and in-plane lattice constant of ZnO (3.34 Å in average) are in good agreement with our STM measurements (~23 Å and 3.3 Å).
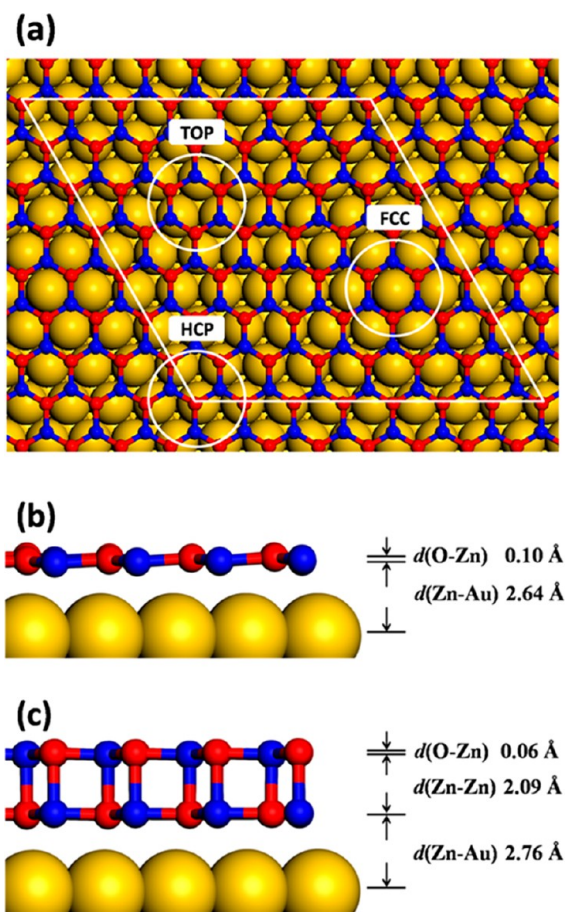

Figure 4. (a) Top view of the single-layer ZnO(0001) on Au(111). The Moiré pattern with periodicity of ZnO(0001)-(7×7)/Au(111)-(8×8) and corresponding FCC, HCP, and TOP domains defined by the sites of Zn on Au(111) are indicated by the white parallelogram and circles, respectively. (b,c) Side views of the optimized structure of the single- and bilayer ZnO(0001) on Au(111), respectively. The average O−Zn rumple d(O−Zn) (in Å) in the topmost ZnO, the average interlayer spacing d(Zn−Zn), and the average spacing d(Zn−Au) between ZnO and Au(111) are indicated. The large yellow ball, small red ball, and blue ball represent Au, O, and Zn, respectively.

For the optimized single-layer ZnO(0001) on Au(111) (Figure 4b), the height difference $d(O-Zn)$ in the surface normal direction between Zn and O atoms (rumple) is 0.10 Å on average (0.14 Å for FCC domain, 0.10 Å for TOP domain, and 0.06 Å for HCP domain) and the average spacing $d(Zn-Au)$ of ZnO from Au(111) is 2.64 Å. For the bilayer ZnO(0001) on Au(111) (Figure 4c), the height difference of normal coordinates between Zn and O atoms in topmost ZnO layer is again very small, 0.06 Å in average (0.07 Å for FCC domain, 0.06 Å for TOP domain, and 0.05 Å for HCP domain). Note that the height difference $d(O-Zn)$ in normal direction between Zn and O atoms in an unreconstructed wurtzite ZnO(0001) layer is 0.63 Å.[10] This indicates that both the single- and bilayer ZnO(0001) on Au(111) adopt the planar, graphite-like structure similar to that seen on Ag(111)[10] and Pd(111).[11] Additionally, the interlayer spacing $d(Zn-Zn)$ between two ZnO layers in the bilayer ZnO(0001) is 2.09 Å, agreeing well with surface X-ray diffraction (SXRD) measurements for planar ZnO films grown on Ag(111) (2.10 Å).[10] This value is 0.51 Å smaller than that of the calculated wurtzite ZnO bulk because both the topmost and lower ZnO layers are planar in the bilayer ZnO(0001). The interlayer spacing $d(Zn-Zn)$ seems in a very good agreement with the apparent height difference of 2 Å measured from the STM experiments. (We caution against directly comparing the physical height and the STM apparent height since the latter involves electronic contributions, which can complicate height estimates.) It should be noted that the bilayer ZnO(0001) with a blend-like stacking (fcc) has also been considered in the calculations, which is shown to be less stable than the wurtzite-like stacking (0.41 eV/ZnO).

The modest rumple (small polarity) and in-plane lattice constant (3.3 Å) of the ZnO(0001) layers on Au(111) indicate a weak interaction between ZnO and Au, as seen from the small interfacial adhesion energy 0.43 eV/ZnO calculated from DFT. In fact, the interfacial adhesion energy is dominated by the van der Waals (vdW) interaction. If the exchange-correlation functional (optB88-vdW)[18] changes to routine GGA-PBE,[25] which inadequately describes the vdW, the calculated interfacial adhesion energy decreases significantly to 0.13 eV/ZnO, and the spatial separation $d(Zn-Au)$ between Zn and Au increases 0.1 Å accordingly. This small interfacial adhesion energy cannot compensate for the energy cost from the existence of a polar surface, so these surface grown ultrathin ZnO(0001) layers follow the depolarization mechanism of the freestanding ZnO(0001) (zero rumple and 3.27 Å). A strong interfacial interaction is needed in order to stabilize a polar surface layer. For instance, for FeO grown on Pt(111), the large interfacial adhesion energy 1.4 eV/FeO is able to compensate and stabilize a polar oxide layer arising from the pronounced O−Fe rumple of 0.68 Å.[26] However, the interlayer interaction between two layers in bilayer ZnO is calculated to be 0.94 eV/ZnO, much larger than the interfacial adhesion energy between ZnO and Au(111). This means that ZnO prefers to stack on each other to form bilayer structure rather than to cover the entire Au(111) surface with the single-layer structure. This explains well the STM observation of the structural transformation from the low-ZnO to high-ZnO during annealing. As such, van der Waals interaction seems to accurately describe the interaction between ZnO layers and their interfacial adhesion with the Au(111) substrate, and the interplay between these two determines the overall bonding between ZnO and Au(111). The strong preference for the ZnO

layers to be oriented exclusively in registry with the Au(111) substrate (as seen in Figure 3) is probably governed by other means (such as an edge effect).

As seen in Figure 3a,b, the experimental STM images could be acquired with no apparent influence of tunneling bias (from 1.5 to 0.2 V). This indicates metallization of the ZnO structures on Au(111) as the bulk wurtzite ZnO is a semiconductor. To understand its metallic origin, a projected density of states (PDOS) of the optimized single-layer ZnO on Au(111) is plotted in Figure 5a. Pronounced PDOS near the Fermi level
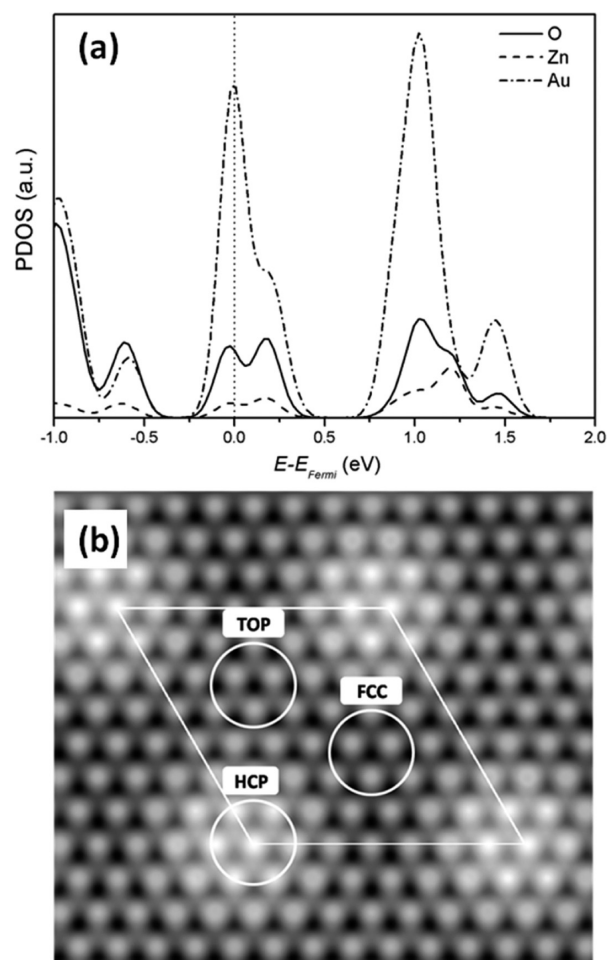

Figure 5. (a) Projected density of states (PDOS) of the single-layer ZnO(0001) on Au(111) near the Fermi level. (b) Simulated STM image of the single-layer ZnO(0001) on Au(111) at a bias of 0.2 eV. The Moiré pattern and corresponding FCC, HCP, and TOP domains are indicated by the white parallelogram and circles, respectively.

from both Au and O are clearly seen, consistent with the metallic behavior of ZnO on Au(111). In contrast, there is a considerable gap (more than 1.5 eV) in the PDOS of the unsupported single-layer ZnO with the same predistorted structure as the supported one (see Figure S1, Supporting Information). This means that the interfacial interaction between ZnO and Au, although relatively weak, is sufficient to modify the electronic structure of the ZnO layer to make it metallic. The simulated STM image at a bias of 0.2 V shown in Figure 5b agrees well with the experimental STM image (Figure 3b). Since oxygen atoms contribute much more states than zinc atoms near the Fermi level (Figure 5a), it is the oxygen atoms that are imaged in STM. The simulated STM
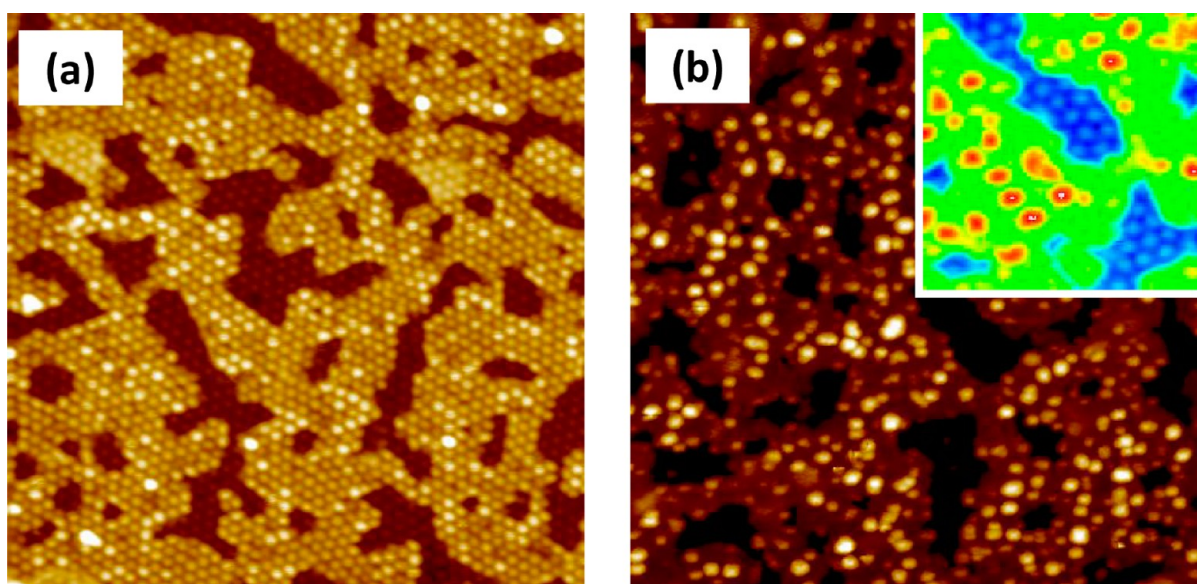
Figure 6. Room temperature STM images of (a) 2 MLE of ZnO grown on Au(111) using the reactive deposition method followed by annealing at 550 K for 120 min, showing a mixture of single- and bilayer ZnO(0001) domains (100×100 nm^2; I = 5 pA, V = 1.5 V); and (b) after the deposition of 0.15 ML Cu, showing that only the bilayer Zn(0001) domains are decorated with Cu species (100×100 nm^2; I = 2 pA, V = −1.5 V). Inset in panel b shows that the single-layer ZnO(0001) domains are free of Cu deposits and that the original hexagonal superstructure remains on the surface after enhancing the image contrast (30×30 nm^2; I = 5 pA, V = 2.0 V).

image also indicates that the brightest areas observed experimentally correspond to the HCP domain of the ZnO layer and the less bright areas to the TOP and FCC domains. These could be better seen in the simulated STM image at a bias of 1.5 eV (Figure S2, Supporting Information).

Despite their structural similarity, the single- and bilayer ZnO(0001) interact differently with Cu. To better demonstrate the differences, we have grown ZnO at higher coverage to form continuous structures. Figure 6a shows an STM image of ∼2 MLE ZnO grown on Au(111) after annealing at 550 K for 120 min to form a mixture of low- and high-ZnO domains. At this coverage, ZnO covers the entire surface of Au(111) with distinguishable domains consisting of the single- and bilayer ZnO(0001). Their height difference is 2 Å, as seen before in nanostructures. The hexagonal Moiré pattern is also visible in both domains with the same periodicity (23 Å). After an evaporation of 0.15 ML of Cu at room temperature (based on an estimate from XPS), STM image shows that the bilayer domains are decorated with many bright features, presumably due to the presence of nanosized Cu particles, whereas no Cu deposits are present on the single-layer ZnO(0001) (Figure 6b). After enhancing the image contrast, the hexagonal superstructure in the single-layer domains also becomes visible (Figure 6b inset), further illustrating that the surface of the single-layer domains does not support the Cu deposits.

The findings above can be rationalized theoretically by the different binding and diffusivity of Cu atoms on the single-layer and bilayer ZnO on Au(111). We find that on the single-layer ZnO (Figure 7a), under its most stable adsorption structure, the Cu atom prefers to be embedded into the oxide layer by substituting one Zn atom and then coordinated with three in-plane O atoms, shown as structure S1 in Figure 7a. The substituted Zn atom is displaced to the intercalated site between the ZnO layer and the Au substrate. The overall adsorption energy with respect to isolated Cu atoms in gas phase is quite large, about −3.24 eV. The embedded configuration and strong binding prohibit the surface diffusion
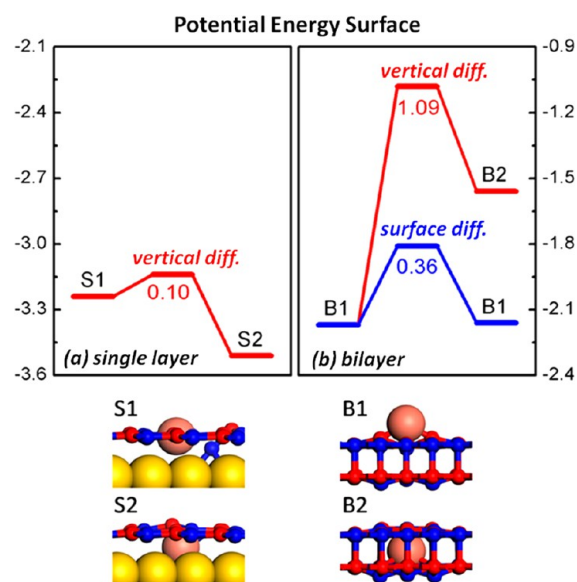

Figure 7. Potential energy surfaces (in eV) of a Cu atom on (a) the single-layer ZnO(0001) on Au(111) and (b) the bilayer ZnO(0001) on Au(111) (the zero energy reference is the isolated Cu atoms in gas phase). On the single-layer ZnO(0001), only the vertical diffusion from Cu atom embedded in ZnO (inset structure S1) to the intercalated site (S2) between ZnO and Au is plotted. On the bilayer ZnO(0001), both the vertical diffusion from Cu atom at the oxygen hollow site (B1) to the intercalated site (B2) between two ZnO layer, and surface diffusion over the surface from B1 to neighbor B1 are plotted. Corresponding barriers for these elementary processes are indicated.

of Cu atom over the single-layer ZnO surface. It can, however, easily diffuse downward to the intercalated site in concert with an upward displacement of the intercalated Zn atom back to its original site in ZnO layer (structure S2 in Figure 7a). The process is exothermic by 0.27 eV and with a very small barrier

of 0.10 eV, which can take place rapidly for instance at room temperature. The intercalated Cu atom could further diffuse downward to the Au subsurface and form Au−Cu alloy with additional energy gain of 0.21 eV. As a result, the single-layer ZnO(0001) is free of Cu species.

Cu atom on the bilayer ZnO(0001) has a completely opposite behavior. Under its most stable adsorption structure, the Cu atom simply sits above the hollow site of three in-plane O atoms (structure B1 in Figure 7b), and the corresponding adsorption energy is −2.17 eV, whose absolute value is 1.07 eV smaller than that on the single-layer ZnO. The relatively weak binding and higher geometrical position indicate that Cu adatoms could be rather mobile. Indeed, we find that the surface diffusion barrier is calculated to be only 0.36 eV. Since the absolute value of adsorption energy of Cu adatoms remains much smaller than that of the cohesive energy of bulk copper (3.76 eV), the mobile Cu adatoms would tend to form clusters or nanoparticles on the bilayer ZnO(0001). Vertical penetration through the topmost ZnO layer into the interstitial sites between ZnO layers (structure B2 in Figure 7b) is, however, endothermic by 0.61 eV with a quite large barrier of 1.09 eV since the relative smaller interlayer spacing (2.09 Å) between the ZnO layers has to be distorted considerably to accommodate the incorporated Cu atom. As such, the Cu atom is metastable and tends to form clusters and/or nanoparticles on the bilayer ZnO(0001).

The differences between the single- and bilayer ZnO(0001) on Au(111) illustrate that the thickness as a controllable dimension can significantly influence characteristics of an ultrathin oxide material. Previously, it has been reported in literature that the quantum confined Pb(111) thin films also exhibit thickness-dependent oxidation and thickness-selective adsorption characteristics.[27] These results suggest that a surface grown ultrathin oxide material could possess versatile properties depending on the number of atomic layers consisting of this material. The ability to precisely control the growth thickness of ultrathin oxide materials could also offer an approach to tailor their structures and tune their properties needed for specific applications, such as selective adoption for separation and chemical sensor applications. Similar to those surface grown α-Fe_2O_3 nanostructures,[28] the ultrathin ZnO(0001) nanostructures on Au(111) also expose significant amounts of edge and interfacial sites, which could lead to enhanced activities toward chemical reactions. These studies are pursued in our group.

CONCLUSIONS

Stoichiometric ZnO is present as either single- or bilayer ZnO(0001) on Au(111), differentiated by their heights in STM. From interplay of experiments based on high-resolution STM and calculations based on DFT, it has been identified that both ZnO structures adopt a planar, graphite-like architecture with the lattice parameters close to a depolarized freestanding ZnO(0001) because the weak van der Waals interaction dominates the interfacial adhesion between both ZnO structures and the Au substrate. The bilayer ZnO(0001) is energetically favored between two structures and becomes more populated after an extended period at 550 K. The driving force behind is that the interaction energy between two ZnO layers is almost twice of the interfacial adhesion energy between ZnO and Au. In addition, the distinct energetics and properties of the single- and bilayer ZnO(0001) associated with adsorption of Cu suggest that tuning the thickness, i.e., the

number of atomic layers, of an ultrathin oxide material may effectively dictate its characteristics.

ASSOCIATED CONTENT

Ⓢ Supporting Information

Details for determining the ZnO stoichiometry based on the XPS data, computational benchmarks, and Figures S1 and S2. This material is available free of charge via the Internet at http://pubs.acs.org.

AUTHOR INFORMATION

Corresponding Author

*E-mail: xingyi.deng@netl.doe.gov (X.D.); wxli@dicp.ac.cn (W.-X.L.).

Author Contributions

‖These authors contributed equally to this work.

Notes

This report was prepared as an account of work sponsored by an agency of the United States Government. Neither the United States Government nor any agency thereof, nor any of their employees, makes any warranty, express or implied, or assumes any legal liability or responsibility for the accuracy, completeness, or usefulness of any information, apparatus, product, or process disclosed, or represents that its use would not infringe privately owned rights. Reference herein to any specific commercial product, process, or service by trade name, trademark, manufacturer, or otherwise does not necessarily constitute or imply its endorsement, recommendation, or favoring by the United States Government or any agency thereof. The views and opinions of authors expressed herein do not necessarily state or reflect those of the United States Government or any agency thereof.

The authors declare no competing financial interest.

REFERENCES

(1) Chambers, S. A.; Droubay, T. C.; Wang, C. M.; Rosso, K. M.; Heald, S. M.; SchwartZ, D. A.; Kittilstved, K. R.; Gamelin, D. R. Ferromagnetism in Oxide Semiconductors. *Mater. Today* **2006**, *9*, 28−35.

(2) Fortunato, E.; Barquinha, P.; Martins, R. Oxide Semiconductor Thin-Film Transistors: A Review of Recent Advances. *Adv. Mater.* **2012**, *24*, 2945−2986.

(3) Baumer, M.; Freund, H. J. Metal Deposits on Well-Ordered Oxide Films. *Prog. Surf. Sci.* **1999**, *61*, 127−198.

(4) (a) Goniakowski, J.; Finocchi, F.; Noguera, C. Polarity of Oxide Surfaces and Nanostructures. *Rep. Prog. Phys.* **2008**, *71*, 55. (b) Nilius, N. Properties of Oxide Thin Films and Their Adsorption Behavior Studied by Scanning Tunneling Microscopy and Conductance Spectroscopy. *Surf. Sci. Rep.* **2009**, *64*, 595−659.

(5) (a) Biener, M. M.; Friend, C. M. Heteroepitaxial Growth of Novel MoO_3 Nanostructures on Au(111). *Surf. Sci.* **2004**, *559*, L173−L179. (b) Deng, X.; Quek, S. Y.; Biener, M. M.; Biener, J.; Kang, D. H.; Schalek, R.; Kaxiras, E.; Friend, C. M. Selective Thermal Reduction of Single-Layer MoO_3 Nanostructures on Au(111). *Surf. Sci.* **2008**, *602*, 1166−1174.

(6) (a) Giordano, L.; Pacchioni, G. Charge Transfers at Metal/Oxide Interfaces: A DFT Study of Formation of $K^{\delta+}$ and Au^δ Species on

MgO/Ag(100) Ultra-Thin Films from Deposition of Neutral Atoms. *Phys. Chem. Chem. Phys.* **2006**, *8*, 3335−3341. (b) Sterrer, M.; Risse, T.; Heyde, M.; Rust, H. P.; Freund, H. J. Crossover from Three-Dimensional to Two-dimensional Geometries of Au Nanostructures on Thin MgO(001) Films: A Confirmation of Theoretical Predictions. *Phys. Rev. Lett.* **2007**, *98*, 206103.

(7) Ellmer, K.; Klein, A.; Rech, B. *Transparent Conductive Zinc Oxide: Basics and Applications in Thin Film Solar Cells*, 1st ed.; Springer: Berlin, Germany, 2008; p 443.

(8) (a) Dulub, O.; Diebold, U.; Kresse, G. Novel Stabilization Mechanism on Polar Surfaces: ZnO(0001)-Zn. *Phys. Rev. Lett.* **2003**, *90*, 016102. (b) Kresse, G.; Dulub, O.; Diebold, U. Competing Stabilization Mechanism for the Polar ZnO(0001)-Zn Surface. *Phys. Rev. B* **2003**, *68*, 245409. (c) Kunat, M.; Girol, S. G.; Burghaus, U.; Woll, C. The Interaction of Water with the Oxygen-Terminated, Polar Surface of ZnO. *J. Phys. Chem. B* **2003**, *107*, 14350−14356. (d) King, S. T.; Parihar, S. S.; Pradhan, K.; Johnson-Steigelman, H. T.; Lyman, P. F. Observation of a $(\sqrt{3} \times \sqrt{3})R30°$ Reconstruction on O-Polar ZnO Surfaces. *Surf. Sci.* **2008**, *602*, L131−L134. (e) Lauritsen, J. V.; Porsgaard, S.; Rasmussen, M. K.; Jensen, M. C. R.; Bechstein, R.; Meinander, K.; Clausen, B. S.; Helveg, S.; Wahl, R.; Kresse, G.; Besenbacher, F. Stabilization Principles for Polar Surfaces of ZnO. *ACS Nano* **2011**, *5*, 5987−5994.

(9) (a) Claeyssens, F.; Freeman, C. L.; Allan, N. L.; Sun, Y.; Ashfold, M. N. R.; Harding, J. H. Growth of ZnO Thin Ffilms: Experiment and Theory. *J. Mater. Chem.* **2005**, *15*, 139−148. (b) Freeman, C. L.; Claeyssens, F.; Allan, N. L.; Harding, J. H. Graphitic Nanofilms as Precursors to Wurtzite Films: Theory. *Phys. Rev. Lett.* **2006**, *96*, 066102.

(10) Tusche, C.; Meyerheim, H. L.; Kirschner, J. Observation of Depolarized ZnO(0001) Monolayers: Formation of Unreconstructed Planar Sheets. *Phys. Rev. Lett.* **2007**, *99*, 026102.

(11) Weirum, G.; Barcaro, G.; Fortunelli, A.; Weber, F.; Schennach, R.; Surnev, S.; Netzer, F. P. Growth and Surface Structure of Zinc Oxide Layers on a Pd(111) Surface. *J. Phys. Chem. C* **2010**, *114*, 15432−15439.

(12) (a) Starr, D. E.; Weis, C.; Yamamoto, S.; Nilsson, A.; Bluhm, H. NO_2 Adsorption on Ag(100) Supported MgO(100) Thin Films: Controlling the Adsorption State with Film Thickness. *J. Phys. Chem. C* **2009**, *113*, 7355−7363. (b) Jung, J.; Shin, H. J.; Kim, Y.; Kawai, M. Controlling Water Dissociation on an Ultrathin MgO Film by Tuning Film Thickness. *Phys. Rev. B* **2010**, *82*, 085413. (c) Carrasco, E.; Brown, M. A.; Sterrer, M.; Freund, H. J.; Kwapien, K.; Sierka, M.; Sauer, J. Thickness-Dependent Hydroxylation of MgO(001) Thin Films. *J. Phys. Chem. C* **2010**, *114*, 18207−18214. (d) Shin, H. J.; Jung, J.; Motobayashi, K.; Yanagisawa, S.; Morikawa, Y.; Kim, Y.; Kawai, M. State-Selective Dissociation of a Single Water Molecule on an Ultrathin MgO Film. *Nat. Mater.* **2010**, *9*, 442−447. (e) Savio, L.; Celasco, E.; Vattuone, L.; Rocca, M. Enhanced Reactivity at Metal-Oxide Interface: Water Interaction with MgO Ultrathin Films. *J. Phys. Chem. B* **2004**, *108*, 7771−7778.

(13) (a) Grunwaldt, J. D.; Molenbroek, A. M.; Topsoe, N. Y.; Topsoe, H.; Clausen, B. S. In Situ Investigations of Structural Changes in Cu/ZnO Catalysts. *J. Catal.* **2000**, *194*, 452−460. (b) Ovesen, C. V.; Clausen, B. S.; Schiotz, J.; Stoltze, P.; Topsoe, H.; Norskov, J. K. Kinetic Implications of Dynamical Changes in Catalyst Morphology during Methanol Synthesis over Cu/ZnO Catalysts. *J. Catal.* **1997**, *168*, 133−142. (c) Klier, K. Methanol Synthesis. *Adv. Catal.* **1982**, *31*, 243−313.

(14) Khan, N. A.; Matranga, C. Nucleation and Growth of Fe and FeO Nanoparticles and Films on Au(111). *Surf. Sci.* **2008**, *602*, 932−942.

(15) Deng, X. Y.; Matranga, C. Selective Growth of Fe_2O_3 Nanoparticles and Islands on Au(111). *J. Phys. Chem. C* **2009**, *113*, 11104−11109.

(16) (a) Kresse, G.; Hafner, J. Ab Initio Molecular Dynamics for Open-Shell Transition Metals. *Phys. Rev. B* **1993**, *48*, 13115−13118. (b) Kresse, G.; Furthmüller, J. Efficient Iterative Schemes for Ab Initio Total-Energy Calculations Using a Plane-Wave Basis Set. *Phys. Rev. B* **1996**, *54*, 11169−11186.

(17) (a) Blöchl, P. E. Projector Augmented-Wave Method. *Phys. Rev. B* **1994**, *50*, 17953−17979. (b) Kresse, G.; Joubert, D. From Ultrasoft Pseudopotentials to the Projector Augmented-Wave Method. *Phys. Rev. B* **1999**, *59*, 1758−1775.

(18) Klimes, J.; Bowler, D. R.; Michaelides, A. Van der Waals Density Functionals Applied to Solids. *Phys. Rev. B* **2011**, *83*, 195131.

(19) Barcaro, G.; Thomas, I. O.; Fortunelli, A. Validation of Density-Functional versus Density-Functional Plus U Approaches for Oxide Ultrathin Films. *J. Chem. Phys.* **2010**, *132*, 124703.

(20) Janotti, A.; Van de Walle, C. G. Native Point Defects in ZnO. *Phys. Rev. B* **2007**, *76*, 165202.

(21) Abad, E.; Dappe, Y. J.; Martínez, J. I.; Flores, F.; Ortega, J. C_6H_6/Au(111): Interface Dipoles, Band Alignment, Charging Energy, and van der Waals Interaction. *J. Chem. Phys.* **2011**, *134*, 044701.

(22) Henkelman, G.; Uberuaga, B. P.; Jonsson, H. A Climbing Image Nudged Elastic Band Method for Finding Saddle Points and Minimum Energy Paths. *J. Chem. Phys.* **2000**, *113*, 9901−9904.

(23) Tersoff, J.; Hamann, D. Theory and Application for the Scanning Tunneling Microscope. *Phys. Rev. Lett.* **1983**, *50*, 1998−2001.

(24) Yeh, J. J.; Lindau, I. Atomic Subshell Photoionization Cross-Sections and Asymmetry Parameters ($1 \leq Z \leq 103$). *At. Data Nucl. Data Tables* **1985**, *32*, 1−155.

(25) Perdew, J. P.; Burke, K.; Ernzerhof, M. Generalized Gradient Approximation Made Simple. *Phys. Rev. Lett.* **1996**, *77*, 3865−3868.

(26) Ouyang, R. H.; Li, W. X. First-Principles Study of the Adsorption of Au Atoms and Au-2 and Au-4 Clusters on FeO/Pt(111). *Phys. Rev. B* **2011**, *84*, 165403.

(27) (a) Ma, X. C.; Jiang, P.; Qi, Y.; Jia, J. F.; Yang, Y.; Duan, W. H.; Li, W. X.; Bao, X.; Zhang, S. B.; Xue, Q. K. Experimental Observation of Quantum Oscillation of Surface Chemical Reactivities. *Proc. Natl. Acad. Sci. U.S.A.* **2007**, *104*, 9204−9208. (b) Jiang, P.; Ma, X. C.; Ning, Y. X.; Song, C. L.; Chen, X.; Jia, J. F.; Xue, Q. K. Quantum Size Effect Directed Selective Self-Assembling of Cobalt Phthalocyanine on Pb(111) Thin Films. *J. Am. Chem. Soc.* **2008**, *130*, 7790−7791.

(28) Deng, X.; Lee, J.; Wang, C.; Matranga, C.; Aksoy, F.; Liu, Z. Reactivity Differences of Nanocrystals and Continuous Films of α-Fe_2O_3 on Au(111) Studied with in Situ X-ray Photoelectron Spectroscopy. *J. Phys. Chem. C* **2010**, *114*, 22619−22623.